

A CONDENSATION–COALESCENCE CLOUD MODEL FOR EXOPLANETARY ATMOSPHERES: FORMULATION AND TEST APPLICATIONS TO TERRESTRIAL AND JOVIAN CLOUDS

KAZUMASA OHNO AND SATOSHI OKUZUMI

Department of Earth and Planetary Sciences, Tokyo Institute of Technology, Meguro, Tokyo, 152-8551, Japan

ABSTRACT

A number of transiting exoplanets have featureless transmission spectra that might suggest the presence of clouds at high altitudes. A realistic cloud model is necessary to understand the atmospheric conditions under which such high-altitude clouds can form. In this study, we present a new cloud model that takes into account the microphysics of both condensation and coalescence. Our model provides the vertical profiles of the size and density of cloud and rain particles in an updraft for a given set of physical parameters, including the updraft velocity and the number density of cloud condensation nuclei (CCN). We test our model by comparing with observations of trade-wind cumuli on the Earth and ammonia ice clouds in Jupiter. For trade-wind cumuli, the model including both condensation and coalescence gives predictions that are consistent with observations, while the model including only condensation overestimates the mass density of cloud droplets by up to an order of magnitude. For Jovian ammonia clouds, the condensation–coalescence model simultaneously reproduces the effective particle radius, cloud optical thickness, and cloud geometric thickness inferred from Voyager observations if the updraft velocity and CCN number density are taken to be consistent with the results of moist convection simulations and Galileo probe measurements, respectively. These results suggest that the coalescence of condensate particles is important not only in terrestrial water clouds but also in Jovian ice clouds. Our model will be useful to understand how the dynamics, compositions, and nucleation processes in exoplanetary atmospheres affects the vertical extent and optical thickness of exoplanetary clouds via cloud microphysics.

Keywords: Earth – planets and satellites: atmospheres – planets and satellites: individual (Jupiter)

1. INTRODUCTION

Recent observations of the transmission spectra of exoplanets revealed that some hot Jupiters (e.g., Pont et al. 2013; Sing et al. 2015, 2016), hot Neptunes (e.g., Crossfield et al. 2013; Ehrenreich et al. 2014; Knutson et al. 2014a; Dragomir et al. 2015; Stevenson et al. 2016), and super-Earth (e.g., Bean et al. 2010; Kreidberg et al. 2014; Knutson et al. 2014b) have featureless spectra. One interpretation of the featureless spectra is that these exoplanets have dust clouds that block starlight at high altitudes (e.g., Seager & Sasselov 2000; Fortney 2005). Dust clouds are also believed to have the crucial impacts on the observed spectra of brown dwarfs whose effective temperature fall into the same range of exoplanets (e.g., Saumon & Marley 2008). For example, the observations of brown dwarfs show a blueward shift of spectral energy distributions during L/T transition that might suggest the sinking of condensate particles (Ackerman & Marley 2001; Burgasser et al. 2002; Marley et al. 2002; Saumon & Marley 2008). Observations also suggest spectral variability that might imply the effect of cloud spatial distributions (Buenzli et al. 2012; Yang et al. 2015, 2016).

A realistic cloud model that predicts the size and spatial distributions of condensation particles for arbitrary atmospheric conditions is necessary to understand the atmospheric properties of both exoplanets and brown dwarfs.

The microphysics that governs the formation of clouds is highly complex, and there are at least two processes by which cloud particles can grow. The first process is the condensation of vapor onto particles in an adiabatically cooling updraft. In terrestrial water clouds and Jovian ice clouds, this process is responsible for the growth of small particles to 10 μm in radius (e.g., Rossow 1978). Further growth of the particles proceeds through the second process, the coalescence driven by the differential settling under gravity. This second process is essential for the initiation of precipitation in terrestrial water clouds (Pruppacher & Klett 1997).

However, previous models of clouds in exoplanets as well as in brown dwarfs neglected or at least parametrized coalescence. The convective cloud model by Ackerman & Marley (2001), which has been used by Morley et al. (2013, 2015) for modeling the transmission spectrum of super-Earth GJ 1214b, encapsulates the effects of particle growth due to condensation and coalescence in a single free parameter f_{sed} . This parameter is given by the ratio of the particle termi-

nal velocity to the atmospheric convective velocity, and depends on the particle size through the terminal velocity. It is commonly assumed that f_{sed} is constant throughout a cloud (Ackerman & Marley 2001; Morley et al. 2013, 2015), but there is no guarantee that it must be for arbitrary convective clouds. The recent cloud model for Earth-like exoplanets by Zsom et al. (2012) treats the microphysics of condensation, but greatly simplifies the coalescence processes by introducing the efficiency of precipitation as a free parameter. The dust cloud model developed by Woitke & Helling (2003, 2004), Helling & Woitke (2006), and Helling et al. (2008), which has recently been applied to clouds in hot Jupiters HD 209458b and HD 189733b (Lee et al. 2015; Helling et al. 2016), takes into account condensation and evaporation but not coalescence. Woitke & Helling (2003) neglected coalescence because, according to Cooper et al. (2003), coalescence takes place much slower than condensation in brown dwarfs. However, as noted by Woitke & Helling (2003), coalescence becomes the only particle growth mechanism even in brown dwarfs if the supersaturation s , defined by the fractional excess of the partial pressure from saturation, is significantly low, e.g., $s \ll 1\%$. While Cooper et al. (2003) fixed the supersaturation to 1%, the actual supersaturation in an updraft depends on the number density of initial condensation nuclei, which is highly uncertain for exoplanets as well as for brown dwarfs.

In this paper, we present a simple one-dimensional cloud model that is simple but takes into account the microphysics of coalescence as well as of condensation. We describe the basic equations and cloud microphysics in our model in Section 2. We test our model by comparing with the observations of the clouds on the Earth and Jupiter in Section 3. We discuss the threshold velocity of sticking and the outlook on application to exoplanetary clouds in Section 4. We present a summary in Section 5.

2. MODEL DESCRIPTION

2.1. Outline

Our model provides the vertical distributions of the mass and number densities of condensate particles (Figure 1). We adopt a one-dimensional Eulerian framework in which the gas ascends at a vertical velocity w . Each condensate particle is assumed to fall relative to the upwelling gas at a terminal speed v_t , which is given by the balance between gas drag and gravity and is therefore a function of the particle radius r (see Equation (A5) for the expression of v_t adopted in this study). Thus, each particle has a net vertical velocity $w - v_t(r)$. We divide the population of condensate particles into small “cloud particles” whose net vertical motion is upward, $w - v_t > 0$, and large “rain particles” whose net vertical motion is downward, $w - v_t < 0$. In this paper, we assume that initial cloud particles form through heterogeneous nucleation (see Section 2.3 for details).

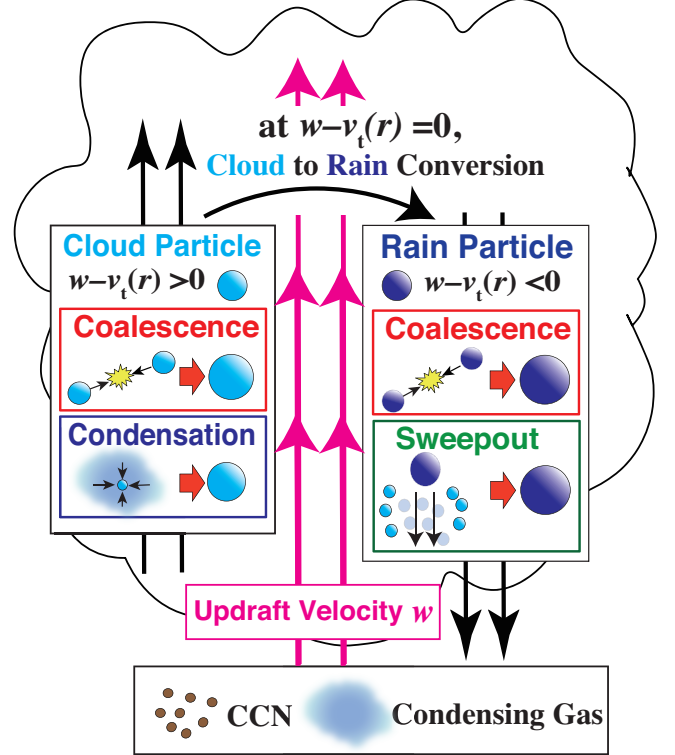


Figure 1. Schematic illustration of our condensation–coalescence cloud model. We consider small “cloud particles” (light blue spheres) and large “rain particles” (dark blue spheres) whose vertical velocity relative to the ground, $w - v_t$, is positive and negative, respectively. The model includes particle growth due to condensation, coalescence, and sweepout (for the definitions of these processes, see Section 2.1), and also vertical transport due to gravitational settling and the updraft motion of the gas.

We denote the total number density and mass density of the cloud (rain) particles by N_c (N_r) and ρ_c (ρ_r), respectively. We assume that the cloud and rain particles have characteristic radii r_c and r_r and characteristic masses $m_c = (4\pi/3)\rho_{\text{int}}r_c^3$ and $m_r = (4\pi/3)\rho_{\text{int}}r_r^3$, respectively, where ρ_{int} is the internal density of the particles. For liquid particles, ρ_{int} is equal to the material density of the condensate, ρ_p , while for solid particles, ρ_{int} can be lower than ρ_p because an aggregate of solid particles can be porous. The porosity of condensate particles can potentially affect the growth and motion of the particles as demonstrated by theoretical studies on dust evolution in protoplanetary disks (e.g., Ormel et al. 2007; Okuzumi et al. 2009). We here neglect this effect by assuming constant bulk density, $\rho_{\text{int}} = \rho_s$, but we plan to take it into account in future work.

Our model determines the vertical distribution of N_c , ρ_c , N_r , ρ_r , and the condensate vapor mass density ρ_v by numerically solving the set of vertically one-dimensional transport equations with terms representing condensation and coalescence (Sections 2.2 and 2.4–2.6). Condensation refers to particle growth through the accretion of supersaturated vapor, while coalescence refers to the growth through collisions with other condensate particles under gravity. In this study,

we refer to the coalescence between cloud and rain particles as sweepout, in order to distinguish the coalescence of two cloud particles or of two rain particles.¹ We neglect the condensation of vapor onto rain particles because the timescale of condensation growth is longer than the timescale of sedimentation for these large particles. The characteristic masses and radii of two particle species (cloud and rain) are automatically determined by the mass and number densities via the relations $m_j = \rho_j/N_j$ and $r_j = (3m_j/4\pi\rho_p)^{1/3}$, respectively, where $j = c$ for cloud particles and $j = r$ for rain particles. Such a framework is called a double-moment bulk scheme in meteorology (e.g., Ziegler 1985; Ferrier 1994), and a characteristic size method in the planet formation community (e.g., Birnstiel et al. 2012; Ormel et al. 2014; Sato et al. 2016). This characteristic size method allows us to simulate the growth of particles with much less computational time than that required with spectral bin schemes where the full size distribution of particles is evolved (Birnstiel et al. 2012; Sato et al. 2016). Our method is particularly useful for studying cloud formation over a wide parameter space.

Because the terminal velocity of particles generally increases as they grow, there is a height $z = z_{\text{top}}$ at which the net upward velocity of cloud particles reaches zero, i.e., $w - [v_t(r_c)]_{z=z_{\text{top}}} = 0$. At this height, which we call the cloud top, we convert the cloud particles into rain particles and allow them to fall and continue growing (see Figure 1). Our implementation of the cloud-to-rain conversion is described in Section 2.7.

2.2. Transport Equations

The transport equations used in our model are given by

$$\frac{\partial N_c}{\partial t} = -\frac{\partial}{\partial z}[(w - v_t(r_c))N_c] - \left. \frac{\partial N_c}{\partial t} \right|_{\text{coal}} - \left. \frac{\partial N_c}{\partial t} \right|_{\text{sweep}}, \quad (1)$$

$$\frac{\partial \rho_c}{\partial t} = -\frac{\partial}{\partial z}[(w - v_t(r_c))\rho_c] + \left(\frac{\partial \rho_c}{\partial t} \right)_{\text{cond}} - m_c \left. \frac{\partial N_c}{\partial t} \right|_{\text{sweep}}, \quad (2)$$

$$\frac{\partial N_r}{\partial t} = -\frac{\partial}{\partial z}[(w - v_t(r_r))N_r] - \left. \frac{\partial N_r}{\partial t} \right|_{\text{coal}}, \quad (3)$$

$$\frac{\partial \rho_r}{\partial t} = -\frac{\partial}{\partial z}[(w - v_t(r_r))\rho_r] + m_c \left. \frac{\partial N_c}{\partial t} \right|_{\text{sweep}}, \quad (4)$$

$$\frac{\partial \rho_v}{\partial t} = -\frac{\partial}{\partial z}(w\rho_v) - \left(\frac{\partial \rho_c}{\partial t} \right)_{\text{cond}}, \quad (5)$$

where $(\partial \rho_c / \partial t)_{\text{cond}}$ is the rate of increase in ρ_c due to condensation, $|\partial N_c / \partial t|_{\text{coal}}$ ($|\partial N_r / \partial t|_{\text{coal}}$) is the rate of decrease in N_c (N_r) due to the coalescence of cloud (rain) particles themselves, and $|\partial N_c / \partial t|_{\text{sweep}}$ is the rate of decrease in N_c due to sweepout. The expressions for $(\partial \rho_c / \partial t)_{\text{cond}}$, $|\partial N_j / \partial t|_{\text{coal}}$, and $|\partial N_c / \partial t|_{\text{sweep}}$ are given in Sections 2.4–2.6.

¹ Sweepout is often termed “accretion” in the literature of cloud microphysical models (e.g., Ziegler 1985).

2.3. Nucleation

We assume that cloud particles form at the cloud base through the condensation of vapor onto small refractory grains that already exist in the atmosphere. This process is known as heterogeneous nucleation, and such refractory grains are termed cloud condensation nuclei (CCN). On Earth CCN include sea salt, ash, and dust from the land (e.g., Rogers & Yau 1989; Seinfeld & Pandis 2006). Lacking information about CCN in other planets including exoplanets, we parametrize them with their number density N_{CCN} and radius r_{CCN} . The CCN number density is a particularly important parameter because it determines the number density and maximum reachable size of cloud particles growing through condensation.

In principle, cloud particles may also form through homogeneous nucleation, where molecules in supersaturated vapor spontaneously collide to form initial nuclei. Although homogeneous nucleation is the simplest nucleation process, this occurs only at a supersaturation ratio much larger than unity because of the free energy barrier arising from the surface tension (e.g., Rogers & Yau 1989; Marley et al. 2013). By contrast, heterogeneous nucleation generally occurs when the supersaturation ratio is slightly above unity because the CCNs lower the free energy barrier (Rogers & Yau 1989). However, if there are only a few CCNs available in the atmosphere, homogeneous nucleation would dominate over heterogeneous nucleation (Woitke & Helling 2004). For simplicity, we ignore homogeneous nucleation in the present study, but we plan to include this effect in our future modeling.

The cloud base is defined by the location above which the saturation vapor pressure P_s of condensing gas under consideration exceeds the partial pressure in the gas phase. This location is mainly determined by the vertical temperature profile of the atmosphere, and weakly depends on the mixing ratio of the condensing gas under the cloud base.

2.4. Condensation

If the cloud particle size r_c is much larger than the mean free path of condensing vapor molecules, the rate of increase in ρ_c due to condensation is given by (Rogers & Yau 1989)

$$\left(\frac{\partial \rho_c}{\partial t} \right)_{\text{cond}} = \frac{4\pi r_c N_c D (\rho_v - \rho_s)}{\left(\frac{L}{R_v T} - 1 \right) \frac{L D \rho_s}{K T} + 1}, \quad (6)$$

where L is the specific latent heat of vaporization, N_c is the number density of the cloud particles, K is the coefficient of thermal conductivity of the atmosphere, and D , R_v , and $\rho_s = \rho_s(T)$ are the diffusion coefficient, specific gas constant, and saturation vapor density of the vapor, respectively. The saturation vapor density is related to the saturation vapor pressure P_s by $\rho_s = P_s / R_v T$. Equation (6) neglects the effects of surface tension and nonvolatile solutes on the saturation vapor pressure over the particles’ surfaces. This

is a good approximation for activated condensate particles (Rogers & Yau 1989).

The assumption that the particle sizes are larger than the atmospheric mean free path is justified for the clouds on the Earth and Jupiter we considered in Section 3. The atmospheric mean free path in the terrestrial water clouds (where $T \approx 300$ K and $P \approx 1$ bar) and in Jovian ammonia clouds (where $T \approx 130$ K and $P \approx 0.5$ bar) is $\sim 0.1 \mu\text{m}$, which is significantly smaller than the typical particle radius in the clouds (see Figures 3 and 5 in Section 3). However, this assumption is not necessarily valid for clouds in exoplanets. For example, ZnS and KCl clouds on super-Earth GJ1214b could form at $P \sim 0.01$ bar (Morley et al. 2013), where the mean free path is $\sim 100 \mu\text{m}$. Furthermore, the observation of GJ1214b suggests the presence of high-altitude clouds at $P \sim 10^{-5}$ bar (Kreidberg et al. 2014; Morley et al. 2015), where the mean free path is as long as $l_g \sim 1$ cm. When one applies our cloud model to such high-altitude clouds, one should replace Equation (6) by the expression in the free molecular regime (for details, see Voitke & Helling 2003),

$$\left(\frac{\partial \rho_c}{\partial t}\right)_{\text{cond}} = 4\pi r_c^2 N_c C_s (\rho_v - \rho_{vs}), \quad (7)$$

where C_s is the mean velocity of gas molecules.

2.5. Coalescence

Under the assumption that the cloud and rain particle size distributions are narrow, the rate of decrease in N_j ($j = c$ or r) due to coalescence is approximately given by

$$\begin{aligned} \left|\frac{\partial N_j}{\partial t}\right|_{\text{coal}} &\approx \frac{1}{2}\pi(r_j + r_j)^2 N_j^2 \Delta v(r_j) E \\ &= 2\pi r_j^2 N_j^2 \Delta v(r_j) E, \end{aligned} \quad (8)$$

where Δv is the relative velocity between the particles induced by gravitational settling, E is the collection efficiency defined by the ratio of the effective collisional cross section to the geometric one (see below). The factor $1/2$ prevents double counting of the collisions. We have used that the geometric collisional cross section between two similar-sized particles is approximately given by $\pi(r_j + r_j)^2$. We express the differential settling velocity as $\Delta v = \epsilon v_t(r_j)$, where the factor $\epsilon (< 1)$ encapsulates the effect of non-zero particle size dispersion. Sato et al. (2016) and Krijt et al. (2016) show that when the differential drift velocity is proportional to the particle size, bulk schemes with $\epsilon \approx 0.5$ best reproduce the results of spectral bin schemes that take into account the full size distribution. In this study, we adopt $\epsilon = 0.5$ for arbitrary values of r_j .

The collection efficiency E accounts for the effect of the gas flow around a large particle moving relative to the background gas: the gas flow sweeps aside particles that are aerodynamically well coupled to the gas (see, e.g., Slinn 1974, Pruppacher & Klett 1997, their Chapter 14). For a collision

between two particles of radii r and r' ($r > r'$), the collection efficiency can be expressed in terms of the Stokes number

$$\text{Stk} = \frac{v_t(r')|v_t(r) - v_t(r')|}{gr}, \quad (9)$$

which is approximately the ratio between the stopping time $= v_t(r')/g$ and crossing time $\sim r/|v_t(r) - v_t(r')|$ of the smaller particle. When $\text{Stk} \ll 1$, the smaller particle is strongly coupled to the flow around the large particle. To zeroth order, E behaves as $E \approx 0$ at $\text{Stk} \ll 1$ and as $E \approx 1$ at $\text{Stk} \gg 1$ (Rossow 1978). In this study, we evaluate E using a smoother analytic function (Guillot et al. 2014, their Equation (99)).

$$E = \max[0, 1 - 0.42 \text{Stk}^{-0.75}], \quad (10)$$

which vanishes at $\text{Stk} \lesssim 0.3$ and approaches unity at $\text{Stk} \gg 1$ (see Figure 12 of Guillot et al. 2014). This expression assumes that flow around the particle is laminar. If the gas flow is turbulent, the collection efficiency can be higher than assumed here (Homann et al. 2016). We approximate Stk in E as $\text{Stk} \approx v_t(r_j)\epsilon v_j/(gr_j)$. Because Stk generally increases with r_j , coalescence occurs only after the particle size exceeds a threshold above which $\text{Stk} > 1$. Therefore, the production of precipitating rain droplets through coalescence requires growth beyond this threshold by condensation (Pruppacher & Klett 1997).

Equation (10) applies when the background gas behaves as a fluid, i.e., the particle radius is much larger than the mean free path of the gas molecules. In the opposite case where the gas behaves as a free molecular flow, one may assume $E = 1$. The free-molecular flow regime is expected to govern the collisional growth of particles at high altitudes where the gas density is low.

2.6. Sweepout

Similar to Equation (8), the rate of decrease in N_c due to sweepout is given by

$$\left|\frac{dN_c}{dt}\right|_{\text{sweep}} = \pi(r_r + r_c)^2 |v_t(r_r) - v_t(r_c)| N_r N_c E. \quad (11)$$

where the collection efficiency E is given by Equation (10) with $\text{Stk} = v_t(r_c)|v_t(r_r) - v_t(r_c)|/(gr_r)$ (see Equation (9)).

2.7. Cloud-to-Rain Conversion

Cloud-to-rain conversion occurs at the height $z = z_{\text{top}}$ where the terminal velocity of cloud particles $v_t(r_c)$ equals the updraft velocity w . Once the terminal velocity of cloud particles exceeds the updraft velocity, we numerically fix the net vertical velocity, $w - v_t(r_c)$, to zero, and let the cloud particles evolve into rain particles at the rate given by $t_{\text{conv}}^{-1} = \beta(t_{\text{cond}}^{-1} + t_{\text{coal}}^{-1})$, where $t_{\text{cond}}^{-1} \equiv (\partial \rho_c / \partial t) / \rho_c$ and $t_{\text{coal}}^{-1} \equiv |\partial N_c / \partial t| / N_c$ are the rates of growth due to condensation and coalescence, respectively, and β is a numerical factor (see also below). The equations that describe the cloud-to-

rain conversion are then given by

$$\left. \frac{\partial N_c}{\partial t} \right|_{z=z_{\text{top}}} = -\frac{N_c}{t_{\text{conv}}}, \quad (12)$$

$$\left. \frac{\partial \rho_c}{\partial t} \right|_{z=z_{\text{top}}} = -\frac{\rho_c}{t_{\text{conv}}}, \quad (13)$$

$$\left. \frac{\partial N_r}{\partial t} \right|_{z=z_{\text{top}}} = \frac{N_c}{t_{\text{conv}}}, \quad (14)$$

$$\left. \frac{\partial \rho_r}{\partial t} \right|_{z=z_{\text{top}}} = \frac{\rho_c}{t_{\text{conv}}}. \quad (15)$$

Strictly speaking, our cloud–rain two-population model breaks down near the cloud top, where the true size distribution of condensate particles (which is not resolved in our model) cannot be approximated with two peaks that are well separated from each other. The numerical factor β we introduced above arises from the lack of information about the continuous particle size distribution from cloud to rain particles. We find that $\beta \gtrsim 1$ –100 causes an oscillating motion of the cloud top that prevents us from obtaining a steady solution. By contrast, $\beta \lesssim 1$ provides a stable steady solution, and we find that the vertical distribution of cloud and rain well below the cloud top is insensitive to the choice of β as long as $\beta \lesssim 1$ (see Section 3.1, 3.2). We will adopt $\beta = 0.1$ in the test simulations presented in the following section.

2.8. Boundary Conditions

The lower boundary of the computational domain is set to the cloud base, which refers to the height above which the saturation ratio $S \equiv \rho_v/\rho_s$ exceeds unity. To determine the location of the cloud base, we introduce the mixing ratio of the cloud-forming vapor below the cloud base as an input parameter. At the cloud base, we set the number density and radius of cloud particles to be equal to those of CCN, N_{CCN} and r_{CCN} , respectively. For rain particles, we simply allow them to leave the computational domain with the (downward) flux determined just above the cloud base.

The upper boundary is taken to be the cloud top, and the boundary conditions at that location are given by Equations (12)–(15). Neither cloud particles nor rain particles are allowed to go above the cloud top because, by definition, the net vertical velocities of the particles vanish at the cloud top.

3. TEST APPLICATIONS

Now we test our cloud model by comparing the observational data of water clouds on the Earth and of ammonia ice clouds on Jupiter. For simplicity, we assume that the vertical structure and updraft motion of the background atmosphere is independent of the presence of clouds. We numerically solve Equations (1)–(5) with Equations (12)–(15), under the fixed boundary conditions at the cloud base, until steady profiles of N_c , ρ_c , N_r , and ρ_r are obtained. To do so, we discretize the vertical coordinate z into linearly spaced bins of width Δz

(10 m for terrestrial water clouds and 20 m for Jovian ammonia clouds), and integrate the equations in time using the first-order explicit scheme.

3.1. Water Clouds on the Earth

We focus on trade-wind cumuli, which are relatively shallow water clouds but are yet deep enough to develop precipitation. vanZanten et al. (2011) conducted comparative studies of terrestrial cloud models using the data of trade-wind cumuli in the northwestern Atlantic ocean obtained from the Rain in Cumulus over the Ocean (RICO) Field Campaign (Rauber et al. 2007). Following vanZanten et al. (2011), we examine how accurately our cloud model reproduces the vertical cloud distribution from the RICO campaign.

Following Weidenschilling & Lewis (1973), we construct the vertical temperature profile by using the dry adiabatic lapse rate ($g/c_p = 9.8 \text{ K km}^{-1}$, where c_p is the specific heat at constant pressure) below the cloud base and the wet adiabatic lapse rate (e.g., the Equation (7) of Atreya et al. 2005) above the cloud base. The vertical pressure profile is calculated by assuming hydrostatic equilibrium (which is a good approximation as long as the updraft motion is slow). In accordance with vanZanten et al. (2011), we fix the surface temperature and CCN number density to 298 K and 70 cm^{-3} , respectively, and adjust the water vapor mixing ratio (or the specific humidity) below the cloud base so that the cloud base is located at 500 m from the ground. The updraft velocity is taken to be either 0.9 m s^{-1} or 2.0 m s^{-1} , which represent the typical updraft velocities in the dense and diffuse parts of the clouds, respectively, in the simulations by vanZanten et al. (2011, their Figure 5).

We approximate the vapor pressure for liquid water with the Arrhenius function

$$p_{s,\text{H}_2\text{O}} = 611 \exp \left[\frac{L}{R_v} \left(\frac{1}{273 \text{ K}} - \frac{1}{T} \right) \right] \text{ Pa}, \quad (16)$$

where the temperature is in K and $L = 2.5 \times 10^6 \text{ J kg}^{-1}$ (Rogers & Yau 1989). The thermal conductivity K and dynamic viscosity η of air are set to $2.4 \times 10^{-2} \text{ W m}^{-1} \text{ K}^{-1}$ and $1.7 \times 10^{-5} \text{ Pa s}$, respectively, and the diffusion coefficient D of water vapor in air is set to $2.2 \times 10^{-5} \text{ m}^2 \text{ s}^{-1}$. These are the values at 273.0 K and 100 kPa (Rogers & Yau 1989). The CCN radius r_{CCN} is assumed to be $0.5 \mu\text{m}$; the results presented below are insensitive to the choice of r_{CCN} as long as it is taken to be smaller than $1 \mu\text{m}$.

Figures 2 and 3 present the results of our test calculations. In Figures 2, we show the steady-state vertical profiles of the number and mass densities of the cloud and rain particles, for $w = 0.9$ and 2.0 m s^{-1} . To highlight the effects of coalescence, we also show the results of simulations without the coagulation and sweepout terms (see the dotted lines). The sizes of the cloud and rain particles as a function of the height z from the ground are shown in Figure 3. In these simulations, the size of the cloud particles reach $\sim 100 \mu\text{m}$

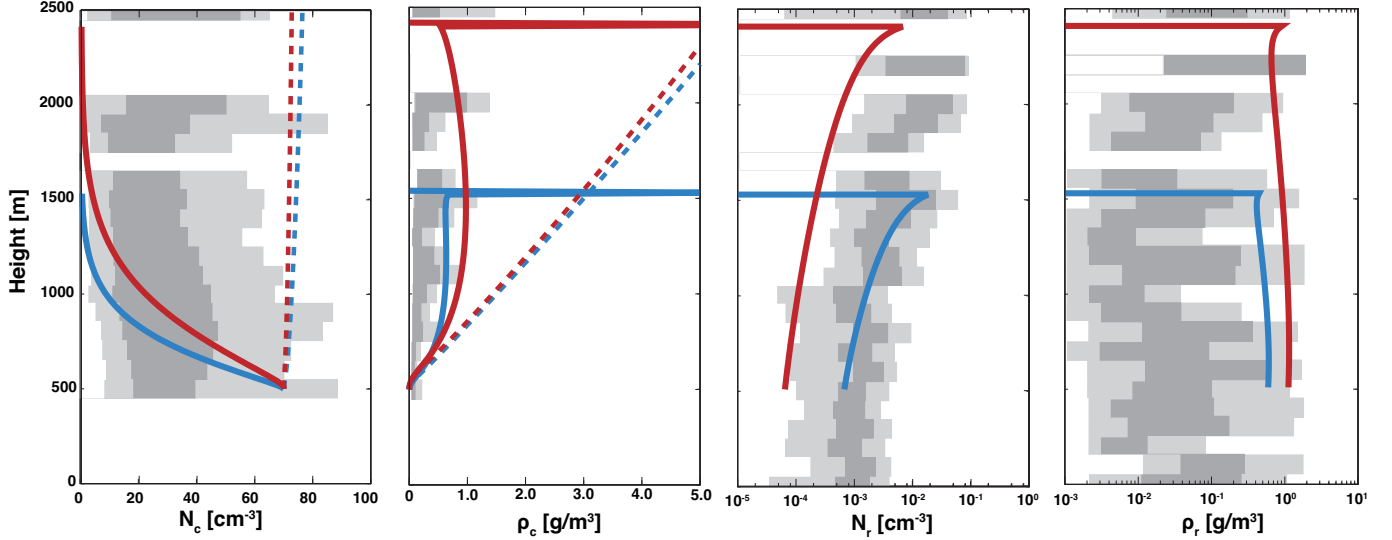


Figure 2. Vertical structure of trade cumulus clouds on the Earth derived from our model calculations as well as from the RICO observations. The four panels show, from left to right, the number and mass densities of cloud particles, N_c , ρ_c , and those of rain particles, N_r , and ρ_r , as a function of the height z from the ground. The blue and red solid lines show the steady-state distributions obtained from our condensation-coalescence model for $w = 0.9$ and 2.0 m s^{-1} , respectively. The dotted lines show the results from the model neglecting coalescence. The light and dark gray-shaded areas span the 5 to 95% and 25 to 75% ranges of the RICO observation data, respectively, taken from Figure 8 of vanZanten et al. (2011).

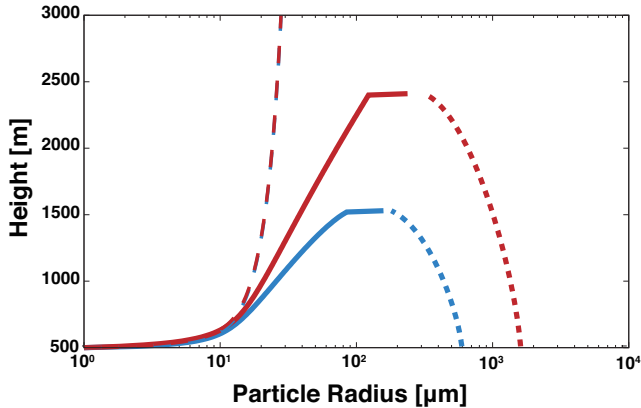


Figure 3. Vertical distributions of the cloud particle radius r_c (solid lines) and rain particle radius r_c (dotted line) from our condensation-coalescence cloud calculations shown in Figure 2. The blue and red lines show the results for $w = 0.9$ and 2.0 m s^{-1} , respectively. The dashed lines show the vertical distribution of the cloud particle radius neglecting coalescence.

at $z \approx 1500 \text{ m}$ for $w = 0.9 \text{ m s}^{-1}$ and at $z \approx 2200 \text{ m}$ for $w = 2.0 \text{ m s}^{-1}$. At these heights, the net vertical velocity $w - v_t(r_c)$ of the cloud particles becomes zero, and we convert them into rain particles that are allowed to continue growing as they fall toward the ground.

Now we compare our simulation results with the RICO flight observations. The light and dark gray-shaded areas in Figure 2 indicate the 5–95% and 25–75% ranges of the observed values, respectively, taken from Figure 8 of vanZanten et al. (2011). Overall, we find that our condensation-coalescence model reproduces the observations to order of magnitude. The predicted values of the cloud

and rain densities fall within the 5–95% range of the observations, except at high altitudes $z \geq 1700 \text{ m}$ where the result for $w = 0.9 \text{ m s}^{-1}$ considerably underestimates the cloud number density. By contrast, the model neglecting coalescence is found to overestimate the mass density of cloud particles by up to an order of magnitude. Furthermore, this condensation-only model fails to reproduce precipitation because the maximum particle size reachable with condensation is too small to fall against an updraft of $w \sim 1 \text{ m s}^{-1}$ (see the dashed lines in Figure 3). With coalescence, cloud particles do grow large enough to start falling as rain particles as we already described above.

Although coalescence resolves the order-of-magnitude discrepancy between the model predictions and observations, the cloud and rain mass densities are still systematically higher than the averages of the observed values. This indicates that the updrafts that produce the observed clouds entrain dry ambient air (e.g., Pruppacher & Klett 1997). Entrainment reduces the temperature and humidity the updraft, both of which act to suppress the condensation growth of cloud particles. The suppressed growth in turn leads to a slower decrease in the cloud number density with height, because coalescence takes place only after the particles grow sufficiently large (see Section 2.5). Therefore, a model including entrainment might better reproduce both the number and mass density of cloud particles. However, the modeling of entrainment within a 1D framework necessarily introduces additional poorly constrained free parameters (see e.g., Pruppacher & Klett 1997, Chapter 12.7, 12.8), which we avoid in this study.

Figures 2 and 3 show that there is a jump in the cloud

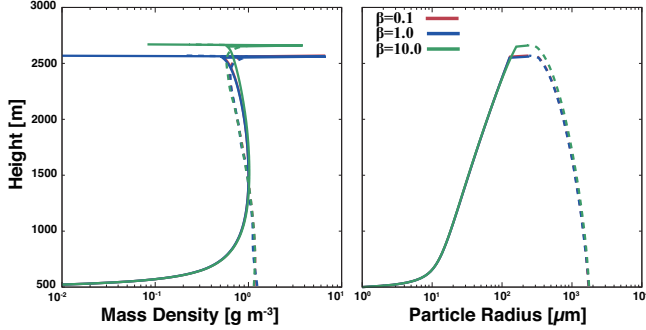


Figure 4. Influences of numerical factor β on the vertical distributions of the cloud particle radius r_c and mass density ρ_c (solid lines), and the rain particle radius r_r and mass density ρ_r (dashed line). The red, blue, and green lines show the simulation results for $\beta = 0.1$, 1.0, and 10.0, respectively. The CCN number densities and updraft velocity are set to $N_{\text{CCN}} = 100 \text{ cm}^{-3}$ and $w = 2.0 \text{ m/s}$.

particle radius and a peak in the cloud mass density at the cloud top. This is an artifact arising from our treatment of the cloud–rain conversion at this location. As emphasized in Section 2.7, our cloud–rain two-population model does not perfectly treat the cloud top where the two populations in reality merge into a single distribution of particles. In fact, we find that the jump and peak features in r_c and ρ_c , as well as the height of the cloud top, weakly depends on the value of the numerical factor β introduced in our cloud–rain conversion calculations. This is shown in Figure 4, where we plot the vertical distributions of the sizes and mass densities of cloud and rain particles for $\beta = 0.1$, 1.0, and 10.0. However, we confirm that this artifact has little effect on the vertical distributions well below the cloud top.

3.2. Ammonia Ice Clouds on Jupiter

We also attempt to reproduce the observations of ammonia clouds on Jupiter. Following Ackerman & Marley (2001), we focus on ammonia ice clouds that cover Jupiter’s upper troposphere where $P \sim 0.7 \text{ bar}$ and $T \sim 130\text{--}140 \text{ K}$ (e.g., West et al. 1986). In accordance with the measurements by the Galileo probe, we model the vertical temperature profile as $T = 166 \text{ K} + \Gamma(z - z_0)$, where $\Gamma = -2 \text{ K km}^{-1}$ is the lapse rate and z_0 is the height at which $P = 1.0 \text{ bar}$ (Seiff et al. 1998), and set the mixing ratio of ammonia gas under the cloud base to be $6.64 \times 10^{-4} \text{ kg kg}^{-1}$ (Wong et al. 2004). The vertical pressure profile is determined under the assumption of hydrostatic equilibrium. We take the updraft velocity and CCN number density as free parameters ranging from 0.1 m s^{-1} to 10 m s^{-1} and from 10^3 m^{-3} to 10^8 m^{-3} , respectively. For the the vapor pressure of ammonia ice, we use the expression by Ackerman & Marley (2001, see also Ackerman & Marley 2013),

$$p_{\text{s,NH}_3} = \exp\left(10.53 - \frac{2161.0}{T} - \frac{86596.0}{T^2}\right) \text{ bar}, \quad (17)$$

where the temperature is in K. The thermal conductivity of the atmosphere is taken to be $K = 9.0 \times 10^{-2} \text{ W m}^{-1} \text{ K}^{-1}$,

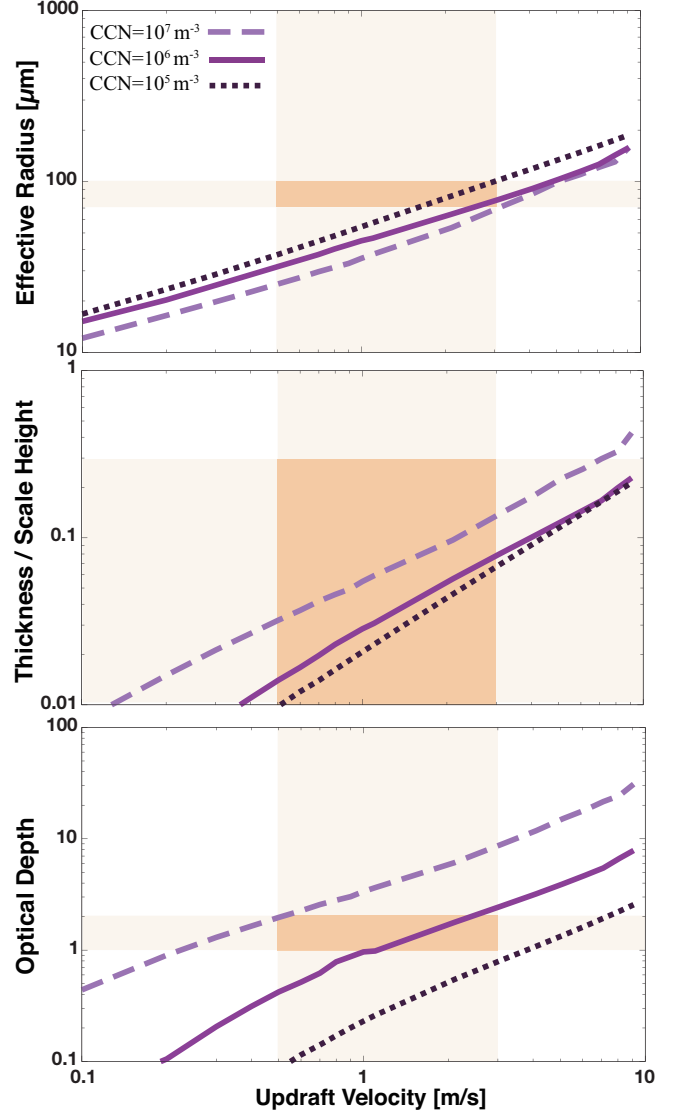


Figure 5. Effective radius r_{eff} (top panel), cloud geometric thickness H_p normalized by pressure scale height H_g , (middle panel), and cloud optical depth τ at visible wavelengths (bottom panel) for Jovian ammonia clouds. The solid lines show the predictions from our condensation–coalescence model for different values of the updraft velocity w (x -axis) and CCN density N_{CCN} (dashed lines for 10^7 m^{-3} , solid lines for 10^6 m^{-3} , and dotted lines for 10^5 m^{-3}). The orange horizontal bars indicate the retrievals from the Voyager IRIS observations by Carlson et al. (1994), while the vertical bars indicate the updraft velocity inferred from the 2D simulations of Jovian moist convection by Sugiyama et al. (2014, their Section 3.1 and Figure 9). The prediction from the condensation–coalescence model satisfies all these constraints when w and N_{CCN} are taken to be $2\text{--}3 \text{ m s}^{-1}$ and $N_{\text{CCN}} \approx 10^6 \text{ m}^{-3}$, respectively.

which is the value for Jovian atmosphere at $T = 134.3 \text{ K}$ (Hansen 1979). The dynamic viscosity of the atmosphere is given by $\eta = 6.7 \times 10^{-6} \text{ Pa s}$ based on the formula for the mixture gas of H_2 and He (Woitke & Helling 2003) together with the assumption $T \approx 130 \text{ K}$. The diffusion coefficient of ammonia gas is given by the formula $D = 2\eta/(3\rho f)$, where ρ is the atmospheric density and $f = 5$ for ammonia vapor (Equa-

tion (14) of Rossow 1978). Following Ackerman & Marley (2001), we take the bulk density of ammonia ice ρ_p to be 0.84 g cm^{-3} . As in the previous subsection, the CCN radius r_{CCN} is assumed to be $0.5 \mu\text{m}$.

We compare the steady-state vertical profiles of the cloud and rain particles obtained from our model with the retrievals by Carlson et al. (1994) based on the infrared observations of Jovian ammonia clouds in the Equatorial Zone and North Tropical Zone from Voyager instrument IRIS. Carlson et al. (1994) retrieved the effective particle radius r_{eff} , geometric thickness H_p , and optical depth τ at the wavelength of $0.5 \mu\text{m}$, where the effective radius refers to the area-weighted average of the radius of visible condensate particles (see, e.g., Kokhanovsky 2004). We evaluate the effective radius in our simulated clouds as

$$r_{\text{eff}} = \frac{\int (r_c^3 N_c + r_r^3 N_r) \exp(-\tau_z) dz}{\int (r_c^2 N_c + r_r^2 N_r) \exp(-\tau_z) dz}. \quad (18)$$

where τ_z is the optical thickness above height z . The factor $\exp(-\tau_z)$ accounts for the fact that one can only observe particles residing at $\tau_z \lesssim 1$. In the calculation of τ and τ_z , we apply the geometric optics approximation to the extinction cross section at visible wavelengths. The geometric thickness of the simulated cloud is taken to be the distance between the cloud base and cloud top in this study.

The results are summarized in Figure 5. Here, the solid lines show the values of r_{eff} , H_p , and τ from our condensation-coalescence model for different sets of the updraft velocity w and CCN density N_{CCN} . The orange horizontal bars indicate the retrievals by Carlson et al. (1994): $r_{\text{eff}} = 70\text{--}100 \mu\text{m}$, $H_p \leq 0.3H_g$, and $\tau = 1.2\text{--}2.0$, where $H_g = 20 \text{ km}$ is the pressure scale height and the range for r_{eff} is based on the interpretation by Ackerman & Marley (2001). We find that the predictions from the condensation-coalescence model satisfies all these observational constraints when the updraft velocity w and CCN number density N_{CCN} are assumed to be $\approx 2\text{--}3 \text{ m s}^{-1}$ and $\approx 10^6 \text{ m}^{-3}$ (see the solid black lines), respectively. If $N_{\text{CCN}} \gtrsim 10^7 \text{ m}^{-3}$ (see the dashed lines), the predicted optical depth falls within the retrieved range only when $w \approx 0.2\text{--}0.5 \text{ m s}^{-1}$; however, for this range of w , the predicted effective radius is too small to be consistent with the retrieval. If $N_{\text{CCN}} \lesssim 10^5 \text{ m}^{-3}$ (see the dotted lines), our prediction reproduces the retrieved optical depth only when $w \approx 3\text{--}7 \text{ m s}^{-1}$, but then overestimates the effective radius from the retrieval.

The results presented in Figure 5 are little affected by the choice of the β parameter introduced in our cloud-top treatment, as shown in Figure 6. One can see that the predictions converge for $\beta \gtrsim 1$. For $\beta = 0.1$, the predicted effective radius and optical depth at $w \gtrsim 0.5 \text{ m/s}$ are higher than the converged values, but the deviation from the converged value is as small as a factor of less than 2.

We compare the updraft velocity of $2\text{--}3 \text{ m s}^{-1}$ with other calculations to validate our best fit value. First, the mix-

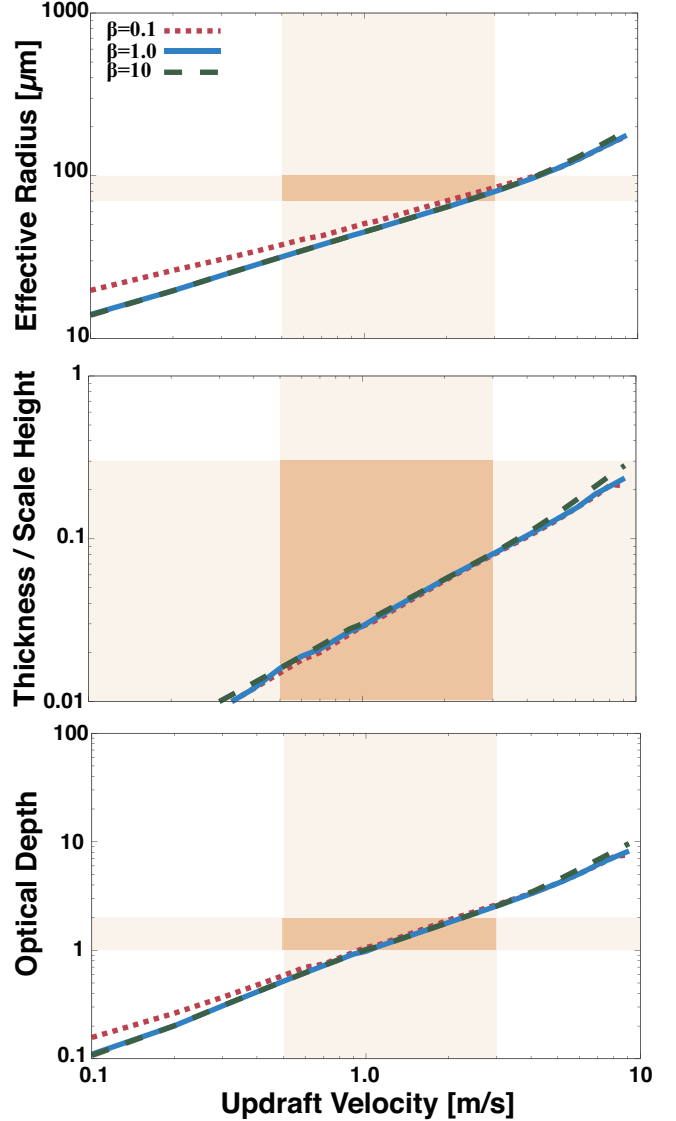


Figure 6. Influence of β on the results for Jovian ammonia ice clouds. The value of N_{CCN} is fixed to 10^6 m^{-3} . The dotted red lines show the simulations for $\beta = 0.1$, the solid blue lines show for $\beta = 1.0$, and the dashed dark-green lines show for $\beta = 10.0$, respectively.

ing length theory formulated by (Ackerman & Marley 2001) suggested the updraft velocity at ammonia cloud region is approximately $1\text{--}3 \text{ m s}^{-1}$, which corresponds to the eddy diffusion coefficient $K_z = 2\text{--}6 \times 10^8 \text{ cm}^2 \text{ s}^{-1}$ and the mixing length equal to $H_g = 20 \text{ km}$. Furthermore, the 2D simulations of the Jovian moist convection show that the updraft velocity at ammonia cloud region is $0.5\text{--}3 \text{ m s}^{-1}$ (Sugiyama et al. 2014) shown in the vertical orange bar of Figure 5. Therefore, our best fit value of updraft velocity of $2\text{--}3 \text{ m s}^{-1}$ is a realistic value for the Jovian ammonia cloud region.

Unfortunately, there is no direct observational constraint on the CCN number density for Jovian ammonia clouds. However, an important hint for the CCN density can be obtained from the in-situ observation of the Jovian atmosphere

in a relatively particle-free hot spot by the Galileo probe. The observation showed that a concentration of small particles of a mean radius of $0.5\text{--}5\ \mu\text{m}$ and a number density of $1.9\times 10^5\text{--}7.5\times 10^6\ \text{m}^{-3}$ was present at a height where ammonia clouds form (Ragent et al. 1998). It is unlikely that the observed particles had experienced coalescence, because the particles are too small to collide with each other (i.e., for particles smaller than a micron in radius, $Stk < 0.5$ and hence $E < 0.3$ in the ammonia cloud forming region). Therefore, we can infer that the number density of CCN, which is approximately equal to the number density of small particles before coalescence sets in, was $\sim 10^5\text{--}10^7\ \text{m}^{-3}$ in the hot spot the Galileo probe entered. Interestingly, this value is consistent with our prediction for the CCN density in the Equatorial Zone and North Tropical Zone (see above). We do not think that this comparison justifies our cloud model, because the CCN density in relatively cloud-free hot spots is not necessarily equal to that in cloudy Equatorial Zone and North Tropical Zone. Rather, this comparison *suggests* that the CCN concentrations in the two regions could be similar.

4. SUMMARY AND OUTLOOK

We have developed a new cloud model for exoplanets and brown dwarfs that is simple but takes into account the microphysics of both condensation and coalescence. Our model produces the vertical distributions of the mass and number densities of cloud and rain particles as a function of physical parameters, including the updraft velocity, the mixing ratio of the condensing gas at the cloud base, and the number density of CCN. Therefore, our model will be useful to understand how the dynamics, compositions, and nucleation processes in exoplanetary atmospheres would affect the vertical structure of exoplanetary clouds via cloud microphysics.

We have tested our model by comparing with the observations of the terrestrial water clouds and the Jovian ammonia clouds. For terrestrial water clouds, our model plausibly reproduces the observed vertical distributions of the cloud mass and number densities from in situ observations when we assume the terrestrial typical updraft velocity, height of cloud base, and CCN number density. For Jovian ammonia clouds, our model simultaneously reproduces the cloud optical depth, the geometric thickness, and the particle effective radius in the Equatorial Zone and North Tropical Zone retrieved from Voyager measurements when we assume the updraft velocity of $w \approx 2\text{--}3\ \text{m s}^{-1}$ and the CCN number density of $N_{\text{CCN}} \approx 10^6\ \text{m}^{-3}$. Our best-fit updraft velocity is consistent with estimates from mixing theory and from cloud convection simulations. The best-fit CCN density is close to the number density of small particles in a hot spot measured by the Galileo probe, suggesting that the CCN density in the Equatorial Zone and North Tropical Zone is similar to that in hot spots. The good agreement between our predictions and the observations indicates that the coalescence of condensate particles is an important process of cloud formation, not only

in terrestrial water clouds but also in Jovian ice clouds.

Equation (8) assumes that two particles stick whenever they collide. However, this assumption breaks down if the collision velocity is so high that the collision results in bouncing or fragmentation of the particles. In principle, solid particles are less sticky than liquid particles because a harder particle has a smaller contact area and hence a small binding energy associated with intermolecular forces (Rossow 1978). Our future modeling will take into account the potentially low sticking efficiency of solid dust particles.

We have also assumed that the internal density of condensate particles is constant. However, the internal density can decrease as the particles grow into porous aggregates through coalescence (e.g., Blum & Wurm 2000). Because porous aggregates have a larger aerodynamical cross section than compact particles of the same mass, porous aggregates might ascend to higher altitudes than compact ones and provide featureless transmission spectra of exoplanetary atmospheres. On the other hand, the coalescence of porous aggregates can be faster than that of compact particles (Okuzumi et al. 2012). If this is the case in exoplanetary atmospheres, the porosity evolution might prevent the formation of high-altitude clouds. Recent theoretical studies of the grain growth in protoplanetary disks have yielded a detailed model for the porosity evolution of grain aggregates based on grain contact mechanics (e.g., Kataoka et al. 2013). We will study the impact of porosity evolution on cloud formation by using these theories in future studies.

The authors thank the anonymous referee for useful comments. We thank Hanii Takahashi and Yuka Fujii for useful discussions about observations of terrestrial clouds, and Chris Ormel for many helpful comments on the manuscript of this paper, and Neal Turner, Shigeru Ida, Masahiro Ikoma, Mark Marley, Yasuto Takahashi, and Xi Zhang for useful comments and discussions. This work is supported by Grants-in-Aid for Scientific Research (#23103005, 15H02065) from MEXT of Japan.

APPENDIX

A. TERMINAL VELOCITY

For particles much larger than the mean free path of the molecules in air, the terminal velocity of a particle under gravity g is given by

$$v_t(r) = \sqrt{\frac{8gr\rho_p}{3C_D\rho_a}}, \quad (\text{A1})$$

where ρ_a is the mass density of the atmosphere, and C_D is the drag coefficient determined by the local Reynolds number of the particle,

$$N_{\text{Re}} \equiv \frac{2rv_t(r)\rho_a}{\eta}, \quad (\text{A2})$$

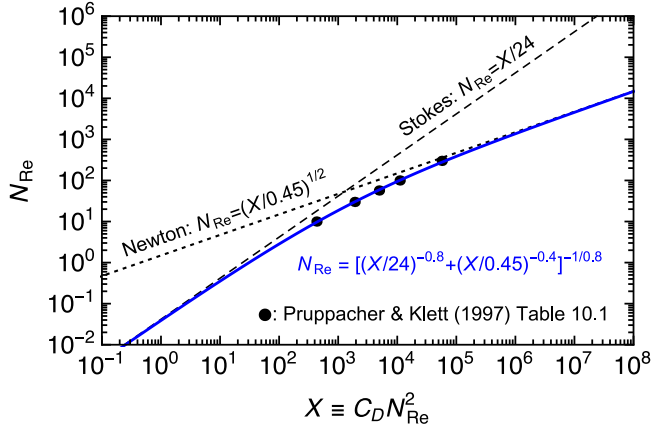


Figure A1. Particle Reynolds number N_{Re} versus $X \equiv C_D N_{\text{Re}}^2$. The dashed and dotted lines indicate the Stokes and Newton drag laws, respectively, and the solid circles show the data for rigid spheres from Table 10.1 of Pruppacher & Klett (1997). The solid line shows our fit, Equation (A4).

where η is the dynamic viscosity of the atmosphere.

Because N_{Re} depends on v_t , one needs to solve Equations (A1) and (A2), together with the relation between C_D and N_{Re} , to obtain v_t as a function of r . Following Ackerman & Marley (2001), we do so by introducing the quantity

$$X \equiv C_D N_{\text{Re}}^2 = \frac{32gr^3\rho_a\rho_p}{3\eta^2}, \quad (\text{A3})$$

which does not involve v_t , and analytically express N_{Re} as a function of X . We require the function to reproduce Stokes' and Newton's drag laws, $C_D = 24/N_{\text{Re}}$ ($N_{\text{Re}} = X/24$) and $C_D = 0.45$ ($N_{\text{Re}} = \sqrt{X/0.45}$), in the limits of $N_{\text{Re}} \ll 1$ and $N_{\text{Re}} \gg 1000$, respectively. To determine the functional form in the intermediate regime $1 \leq N_{\text{Re}} \leq 1000$, we use the data for rigid spheres from Table 10.1 of Pruppacher & Klett (1997). We find that the function

$$N_{\text{Re}} = \left[\left(\frac{X}{24} \right)^{-0.8} + \left(\frac{X}{0.45} \right)^{-0.4} \right]^{-1/0.8} \quad (\text{A4})$$

well reproduces the data points in the intermediate regime and the correct limiting behaviors at $N_{\text{Re}} \ll 1$ and $N_{\text{Re}} \gg 1000$ (see Figure A1). Substituting this expression and Equation (A3) into Equation (A2), we obtain the analytic expression for v_t as a function of r ,

$$v_t = \frac{2gr^2\rho_p}{9\eta} \left[1 + \left(\frac{0.45gr^3\rho_a\rho_p}{54\eta^2} \right)^{0.4} \right]^{-1.25}. \quad (\text{A5})$$

If the particles are small the atmospheric mean free path, one should use the Epstein law

$$v_t(r) = \frac{g\rho_p}{3C_s\rho_a} r \quad (\text{A6})$$

instead of Equation (A5). This is the case for high-altitude clouds in exoplanets (see Section 2.4).

REFERENCES

- Ackerman, A. S., & Marley, M. S. 2001, *ApJ*, 556, 872
 Ackerman, A. S., & Marley, M. S. 2013, *ApJ*, 765, 75
 Atreya, S. K., & Wong, A.-S. 2005, *SSRv*, 116, 121
 Bean, J. L., Miller-Ricci Kempton, E., & Homeier, D. 2010, *Nature*, 468, 669
 Birnstiel, T., Klahr, H., & Ercolano, B. 2012, *A&A*, 539, A148
 Blum, J., & Wurm, G. 2000, *Icarus*, 143, 138
 Buenzli, E., Apai, D., Morley, C. V., et al. 2012, *ApJL*, 760, L31
 Burgasser, A. J., Marley, M. S., Ackerman, A. S., et al. 2002, *ApJL*, 571, L151
 Carlson, B. E., Lacis, A. A., & Rossow, W. B. 1994, *J. Geophys. Res.*, 99, 14
 Cooper, C. S., Sudarsky, D., Milsom, J. A., Lunine, J. I., & Burrows, A. 2003, *ApJ*, 586, 1320
 Crossfield, I. J. M., Barman, T., Hansen, B. M. S., & Howard, A. W. 2013, *A&A*, 559, A33
 Dragomir, D., Benneke, B., Pearson, K. A., et al. 2015, *ApJ*, 814, 102
 Ehrenreich, D., Bonfils, X., Lovis, C., et al. 2014, *A&A*, 570, A89
 Ferrier, B. S. 1994, *J. Atmos. Sci.*, 51, 249
 Fortney, J. J. 2005, *MNRAS*, 364, 649
 Guillot, T., & Ormel, C. W. 2014, *A&A*, 572, A72
 Hansen, C. F. 1979, NASA Technical Memo 78556
 Helling, Ch., & Woitke, P. 2006, *A&A*, 455, 325
 Helling, C., Woitke, P., & Thi, W.-F. 2008, *A&A*, 485, 547
 Helling, C., Lee, G., Dobbs-Dixon, I., et al. 2016, *MNRAS*, 460, 855
 Homann, H., Guillot, T., Bec, J., et al. 2016, *A&A*, 589, A129
 Kataoka, A., Tanaka, H., Okuzumi, S., & Wada, K. 2013, *A&A*, 554, A4
 Kokhanovsky, A. 2004, *Earth-Science Reviews*, 64, 189
 Knutson, H. A., Benneke, B., Deming, D., & Homeier, D. 2014, *Nature*, 505, 66
 Knutson, H. A., Dragomir, D., Kreidberg, L., et al. 2014, *ApJ*, 794, 155
 Kreidberg, L., Bean, J. L., Désert, J.-M., et al. 2014, *Nature*, 505, 69
 Krijt, S., Ormel, C. W., Dominik, C., & Tielens, A. G. G. M. 2016, *A&A*, 586, A20
 Lee, G., Helling, C., Dobbs-Dixon, I., & Juncher, D. 2015, *A&A*, 580, A12
 Marley, M. S., Seager, S., Saumon, D., et al. 2002, *ApJ*, 568, 335
 Marley, M. S., Ackerman, A. S., Cuzzi, J. N., & Kitzmann, D. 2013, *Comparative Climatology of Terrestrial Planets*, 367
 Morley, C. V., Fortney, J. J., Kempton, E. M.-R., et al. 2013, *ApJ*, 775, 33
 Morley, C. V., Fortney, J. J., Marley, M. S., et al. 2015, *ApJ*, 815, 110
 Okuzumi, S., Tanaka, H., & Sakagami, M.-a. 2009, *ApJ*, 707, 1247
 Okuzumi, S., Tanaka, H., Kobayashi, H., & Wada, K. 2012, *ApJ*, 752, 106
 Ormel, C. W. 2014, *ApJ*, 789, L18
 Ormel, C. W., Spaans, M., & Tielens, A. G. G. M. 2007, *A&A*, 461, 215
 Pont, F., Sing, D. K., Gibson, N. P., et al. 2013, *MNRAS*, 432, 2917
 Pruppacher, H. R., & Klett, J. D. 1997, *Microphysics of Clouds and Precipitation* (Dordrecht: Kluwer)
 Ragent, B., Colburn, D. S., Rages, K. A., et al. 1998, *J. Geophys. Res.*, 103, 22891
 Rauber, R. M., Stevens, B., Ochs, H. T., et al. 2007, *Bull. Amer. Meteor. Soc.*, 88, 1912
 Rogers, R., & Yau, M. 1989, *A Short Course in Cloud Physics* (3rd ed.; Oxford: Butterworth-Heinemann)
 Rossow, W. B. 1978, *Icarus*, 36, 1
 Sato, T., Okuzumi, S., & Ida, S. 2016, *A&A*, 589, A15
 Saumon, D., & Marley, M. S. 2008, *ApJ*, 689, 1327-1344
 Seager, S., & Sasselov, D. D. 2000, *ApJ*, 537, 916
 Seinfeld, J. H., & Pandis, S. N. 2006, *Atmospheric Chemistry and Physics: From Air Pollution to Climate Change* (2nd ed.; New Jersey: Wiley)
 Seiff, A., Kirk, D. B., Knight, T. C. D., et al. 1998, *J. Geophys. Res.*, 103, 889, 22822

- Sing, D. K., Wakeford, H. R., Showman, A. P., et al. 2015, *MNRAS*, 446, 2428
- Sing, D. K., Fortney, J. J., Nikolov, N., et al. 2016, *Nature*, 529, 59
- Slinn, W. G. N. 1974, *Proceedings of the USAEC Symposium*
- Stevenson, K. B., Bean, J. L., Seifahrt, A., et al. 2016, *ApJ*, 817, 141
- Sugiyama, K., Nakajima, K., Odaka, M., Kuramoto, K., & Hayashi, Y.-Y. 2014, *Icarus*, 229, 71
- VanZanten, M. C., Stevens, B., Nuijens, L., et al. 2011, *J. Advances in Modelling Earth System*, 3, M06001
- Weidenschilling, S. J., & Lewis, J. S. 1973, *Icarus*, 20, 465
- West, R. A., Strobel, D. F., & Tomasko, M. G. 1986, *Icarus*, 65, 161
- Woitke, P., & Helling, C. 2003, *A&A*, 399, 297
- Woitke, P., & Helling, C. 2004, *A&A*, 414, 335
- Wong, M. H., Mahaffy, P. R., Atreya, S. K., Niemann, H. B., & Owen, T. C. 2004, *Icarus*, 171, 153
- Yang, H., Apai, D., Marley, M. S., et al. 2015, *ApJL*, 798, L13
- Yang, H., Apai, D., Marley, M. S., et al. 2016, *ApJ*, 826, 8
- Ziegler, C. L., 1985, *J. Atmos. Sci.*, 42, 1487
- Zsom, A., Kaltenegger, L., & Goldblatt, C. 2012, *Icarus*, 221, 603.